

Contact mechanics of and Reynolds flow through saddle points

On the coalescence of contact patches and the leakage rate through near-critical constrictions

WOLF B. DAPP¹ and MARTIN H. MÜSER^{1,2}

¹ *Supercomputing Centre Jülich, Institute for Advanced Simulation, FZ Jülich, 52425 Jülich, Germany*

² *Lehrstuhl für Materialsimulation, Universität des Saarlandes, 66123 Saarbrücken, Germany*

PACS 46.55.+d – Tribology and mechanical contacts

PACS 68.35.-p – Solid surfaces and solid-solid interfaces: structure and energetics

Abstract – We study numerically local models for the mechanical contact between two solids with rough surfaces. When the solids softly touch either through adhesion or by a small normal load L , contact only forms at isolated patches and fluids can pass through the interface. When the load surpasses a threshold value, L_c , adjacent patches coalesce at a critical constriction, i.e., near points where the interfacial separation between the undeformed surfaces forms a saddle point. This process is continuous without adhesion and the interfacial separation near percolation is fully defined by scaling factors and the sign of $L_c - L$. The scaling factors lead to a Reynolds flow resistance which diverges as $(L_c - L)^{-\beta}$ with $\beta = 3.45$. Contact merging and destruction near saddle points becomes discontinuous when either short-range adhesion or specific short-range repulsion are added to the hard-wall repulsion. These results imply that coalescence and break-up of contact patches can contribute to Coulomb friction and contact aging.

Introduction. – When two nominally rough solids are pressed against each other, their surfaces tend to touch microscopically only at isolated points [1, 2]. Simple models assume that real contact between two rough surfaces can be decomposed into single-asperity, Hertzian-like contacts. However, both experiment [3, 4] and large-scale simulations [5–9] have revealed that the majority fraction of contiguous contact patches appear to be fractal and to result from many (formerly) single-asperity contacts. While the latter are well studied, less is known about the way in which they merge [10–13], in particular when adhesion is present. For example, it is unclear if adhesive contact-patch coalescence and break-up happen discontinuously. Contact-patch coalescence also plays a role for seals: it has been argued that their leakage rate is determined to a significant degree from the topology of the last critical constriction [14], i.e., the neighborhood of the point, which, upon increasing load or adhesion, is the first point to interrupt a percolating non-contact path.

In this work, we study local models for the merging of contact patches, or, in the context of seals, the contact mechanics of critical constrictions. The local gap topography of a critical constriction is such that the interfacial separation of the undeformed surfaces is (close to) a saddle point. More precisely, near the percolation point, the gap is very small. Parallel to a just-blocked fluid channel,

the gap opens, while in the orthogonal, in-plane direction, the gap is closed, because the interfacial separation of the undeformed surfaces decreases in that direction. Thus, studying the contact mechanics of saddle points entails the analysis of critical constrictions and that of contact patch merging. Here, we investigate not only the contact mechanics of (near-) critical constrictions, including a scaling analysis of the gap topography near the percolation point, but also address the pertaining Reynolds flow with and without adhesion.

To simulate the contact mechanics of an isolated saddle point, we reinvestigate rather simple models [10, 11, 13] for the (combined) surface roughness and for the interactions between the surfaces. Yet, in addition to the hard-wall repulsion commonly assumed infinitely short-ranged in continuum mechanics, we also study the effects of finite-range attraction [15] and repulsion [16] between the surfaces. Our motivation for additional repulsion stems from recent simulations, in which appropriately designed cohesive-zone models qualitatively reproduced the surface interactions mediated by a strongly wetting fluid inducing an effective negative surface energy of finite range [16]. The length-scale of these additional surface interactions is nevertheless short enough for interfacial interactions not to act far away from a contact line, i.e., our Tabor parameters [15] are $\gg 1$.

Models and Methods. — We assume linear elasticity and the small-slope approximation so that roughness can be mapped to a rigid substrate and the elastic compliance to a flat counter body. The effective contact modulus is used to define the unit of pressure, i.e., $E^* = 1$. Elasticity is treated with Green’s function molecular dynamics (GFMD) [17] and the continuum version of the stress-displacement relation in Fourier space, $\tilde{\sigma}(\mathbf{q}) = qE^*\tilde{u}(\mathbf{q})/2$, where \mathbf{q} is a wave vector and q its magnitude. Simulations are run in a force-controlled fashion. After the external load has changed by a small amount, all degrees of freedom are relaxed until convergence is attained.

Three models for the (combined) height profiles are employed. Each profile has roughness only at a single wavelength λ , a root-mean-square height fluctuation of h_0 , and a root-mean-square gradient of $2\pi h_0/\lambda$, which should be small enough for the small-slope approximation to be valid. In other words, all three lattices yield identical angle-averaged spectra at non-zero wave numbers. First, we consider a square lattice

$$\frac{h_{sq}(x, y)}{h_0} = 2 + \cos\left(\frac{2\pi x}{\lambda}\right) + \cos\left(\frac{2\pi y}{\lambda}\right), \quad (1)$$

for which the simulation cell dimensions along x and y direction are chosen to coincide with the wavelength λ of the height undulation, that is $L_x = L_y = \lambda$. The two remaining lattices are triangular and hexagonal:

$$\begin{aligned} \frac{h_{tl}(x, y)}{h_0} = & \sqrt{\frac{2}{3}} \left\{ \frac{3}{2} + 2 \cos\left(\frac{\sqrt{3}\pi x}{\lambda}\right) \cos\left(\frac{\pi y}{\lambda}\right) \right. \\ & \left. + \cos\left(\frac{2\pi y}{\lambda}\right) \right\} \quad (\text{hexagonal lattice}) \quad (2) \end{aligned}$$

$$\frac{h_{hl}(x, y)}{h_0} = \sqrt{\frac{27}{2}} - \frac{h_{tl}(x, y)}{h_0} \quad (\text{triangular lattice}) \quad (3)$$

for which the dimensions of the periodically repeated simulation cells are $L_x = 4\lambda/\sqrt{3}$ and $L_y = 2\lambda$. This shape is relatively close to a square so that discretization corrections [18] are almost isotropic in our GFMD calculations, which decomposes the surfaces into $2^n \times 2^n$ elements.

In each model, the height offset is set to yield a minimum height of zero. Other key geometrical attributes are: Maximum height ($\sqrt{27/2} h_0$, $4 h_0$, $\sqrt{27/2} h_0$), mean trough depth ($\sqrt{6} h_0$, $2 h_0$, $\sqrt{2/3} h_0$), skewness ($-\sqrt{2/3}$, 0 , $\sqrt{2/3}$), and excess kurtosis ($-1/2$, $-3/4$, $-1/2$), each time in the order hexagonal, square, and triangular lattice.

Two surfaces interact with a hard-wall constraint, i.e., they are not allowed to overlap. In addition we assume cohesive zone models for the finite-range interactions between the surfaces. It is $\gamma = -\gamma_0 \exp\{-g/\rho\}$ for attractive forces, where $g = g(x, y)$ is the local gap or interfacial separation. Typical values for both γ_0 and ρ are small numbers in the appropriate unit system, e.g., $\gamma_0 = 0.2 E^* h_0^2/\lambda$ and $\rho = 0.04 h_0$. To give one possible realization: If E^* were 1 GPa, $h_0 = 10$ nm, and $\lambda = 1 \mu\text{m}$, then $\gamma_0 = 20$ mN/m, which reflects the order of magnitude for

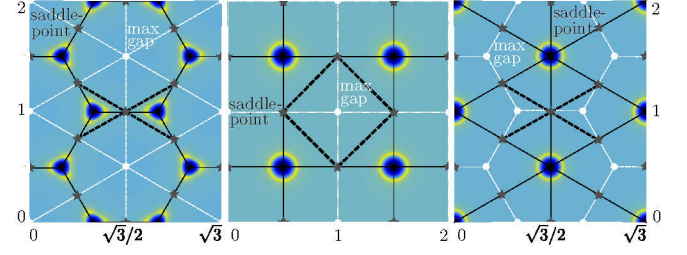


Fig. 1: Elastic displacements at zero load for the hexagonal, square, and triangular substrate lattice, from left to right. Dark colors represent small displacements, that is, points of contact. These are enveloped by yellow halos indicative of localized, adhesive necks. Thin black lines connect substrate height maxima, while thin white lines connect substrate height minima or troughs, which are marked by white points. Grey stars reflect saddle points. Only selected lines between nearest-neighbor saddle points are drawn (thick dotted lines).

the surface energy of flat, non-polar, and chemically passivated surfaces. Finite-range repulsion is modeled with a different functional form than adhesion, namely with $\gamma(x, y) = -\gamma_0 \exp\{-g(x, y)^2/2\rho^2\}$. The detailed rationale for these functional forms is given elsewhere [16]. In brief: the exponential adhesive model mimics the large Tabor number limit quite efficiently while allowing one to determine contact area in an unambiguous manner. The Gaussian repulsive interactions can simulate the effect of a last layer, which needs to be squeezed out before two surfaces touch.

Figure 1 conveys an impression of our models. It shows the elastic displacement for the investigated symmetries in case of adhesion and zero external load. The dark areas show the locations of small displacement and thereby the structure of initial contact patches. The halos around contact points reflect bulges near the contact line that are well known from single-asperity contacts with short-range adhesion. One can also recognize that the displacements are rather constant near the height minima. The latter lie on lattices dual to the height maxima for the considered cases. For example, the height minima (or gap maxima) form a triangular lattice when the substrate heights lie on a hexagonal lattice, and vice versa. Saddle points form a kagome lattice in these two cases. For the square lattice, not only height maxima but also minima and saddle points each form a square lattice.

Flow through the interface is described by Reynolds thin-film equation, which assumes a local conductivity that scales as the inverse third power of the gap. We use the **hypre** package [19] to solve the sparse linear system that the discretized Reynolds equation can be expressed as. We employ the solvers supplied with **hypre** using the CG (conjugate gradient), or GMRES (generalized minimal residual) methods [20], each preconditioned using the PFMG method, which is a parallel semicoarsening multi-grid solver [21]. Our in-house code is MPI-parallelized and uses HDF5 for I/O.

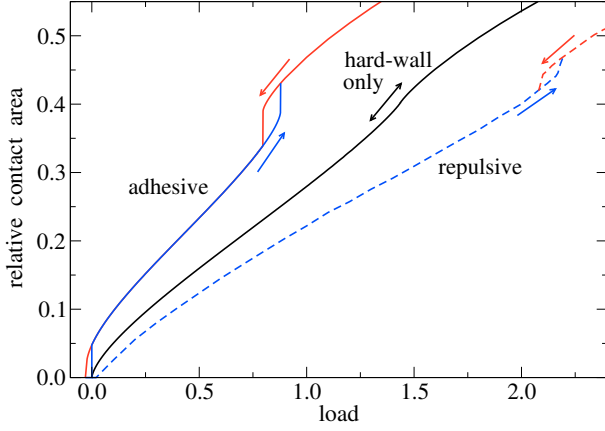


Fig. 2: Relative contact area as a function of load for the square-lattice substrate and different finite-range interactions. Red (blue) lines refer to increasing (decreasing) external load as marked by arrows. Exponential adhesion (solid lines) and Gaussian repulsion (dashed lines) show the established hystereses at small contact area related to contact formation. Unless solids interact solely by hard-wall repulsion, additional hystereses appear at relative contact areas near 0.4. They reflect the contact-patch-coalescence and break-up instabilities.

Results. — A central question addressed in this study is whether the merging of two contact patches happens continuously or discontinuously. Figure 2 confirms previous findings [10, 13] that percolation is continuous when surfaces interact solely with hard-wall repulsion. However, once finite-range repulsion (with the functional form defined in the method section) or short-range attraction is added, contact patches and likewise fluid channels coalesce and break up through instabilities. The behavior is qualitatively similar for the two remaining models, despite large quantitative differences.

Contacts also coalesce discontinuously when driven entirely by adhesion. This is revealed in Figure 3. Despite similar conditions — identical adhesion and surface spectra — the quantitative differences between the three models are clearly borne out: The hexagonal (triangular) lattice has by far the largest (smallest) propensity to form a coalesced or percolated contact area. This is because its peaks are rather blunt or obtuse (pointed or acute) and the ridges connecting the peaks have small (large) curvature. However, the hexagonal (triangular) lattice has the smallest tendency to go into full contact, because its troughs are rather deep (shallow) and the curvature normal to the ridges are large (small) in magnitude. In the triangular lattice, the propensity to form full contact is even so large that partial, coalesced contact is not even metastable at finite adhesion and zero load. The square model is somewhere in between the two extreme cases.

While adhesion-free/load-driven and adhesion-driven/load-free percolation are qualitatively different in that the former is continuous and the latter is discontinuous, they happen at similar relative contact areas.

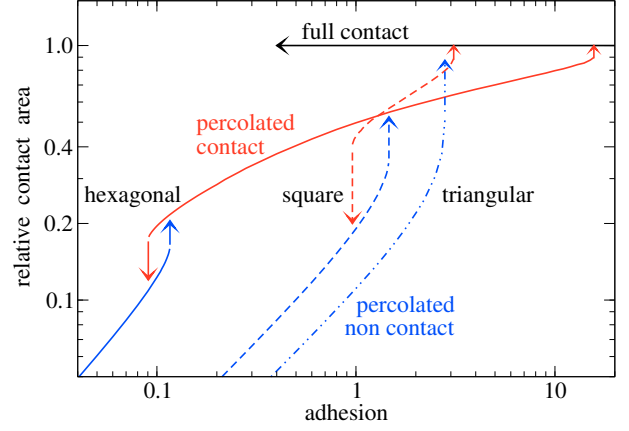


Fig. 3: Relative contact area as a function of surface energy γ_0 for the three investigated models. The instabilities at lower values of γ_0 are related to percolation transitions. The single-wavelength, triangular substrate circumvents the percolated, partial contact regime by transitioning directly from isolated contact patches to full contact.

The precise values in the purely load-driven case with only hard-wall repulsion are $a_p = 0.17826(11)$ (triangular lattice), $0.40185(6)$ (square lattice), and $0.67323(1)$ (hexagonal lattice). Interestingly, the average of these numbers (0.418) is close to the percolation threshold identified for self-affine, isotropic, randomly-rough and non-adhesive bodies (0.425) [22]. In the adhesion-driven case, the percolation of contact is triggered at relative contacts slightly below the given values of a_p and ends at values slightly above a_p . The reverse transitions from partial but coalesced to isolated contact patches also occur near the respective values for a_p , though shifted to slightly smaller values.

While only peripheral to this work, we briefly discuss the transition to full contact. In the purely force-driven case, full contact occurs above critical mean pressures of $p_{fc} = \pi E^* \bar{t} / \lambda$, where \bar{t} is the mean trough depth (stated in the model section). This relation is readily obtained from the single-wavelength, full-contact solution [10]. (In the original work, an additional factor of $\sqrt{2}$ was included, as the wavelength was defined to be $\lambda/\sqrt{2}$.) The purely adhesion-driven percolation roughly follows the force-driven percolation, e.g., the ratio γ_{fc}/γ_p is largest for the hexagonal (135) and smallest for the triangular (1) model. Pertinent ratios for the critical forces in the absence of adhesion are 31 (hexagonal) and 1.4 (triangular). Here and in the following, we do not address the reverse transition from full to partial contact for adhesive surfaces, because it would correspond to a Griffith-like fracture problem lacking an initial crack. As such, for our and related adhesive laws, full contact becomes unstable at tensile pressure $\lesssim \gamma_0/\rho$. The other adhesion-related results presented here barely depend on the precise choice of ρ as long as $\rho \ll h_0$.

The above results reveal a quite significant influence of local structure on prefactors. Some of the differences can

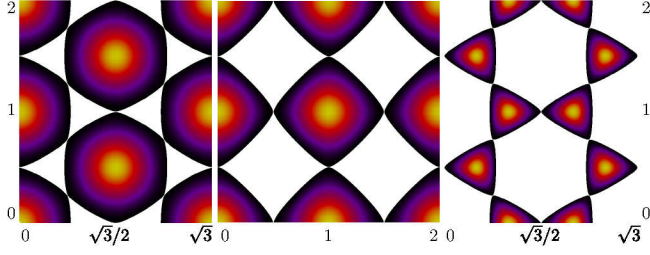


Fig. 4: Gaps (in color, where bright colors indicate large gaps and dark color small gaps) and contact (white) near the percolation threshold for the three investigated geometries. Systems are arranged in the same way as in Figure 1.

be rationalized from the contact and gap geometries near the percolation threshold, which are depicted in Figure 4 for simple hard-wall repulsion. In coarse-grained representations the impression is conveyed that, depending on geometry, opening angles can range from acute to obtuse.

Locally, however, all investigated saddle points are similar in that they sit at points of inversion symmetry, the curvatures of the substrate heights parallel to the fluid-channel ($h''_{||}$) are negative and those in orthogonal, in-plane direction (h''_{\perp}) are positive. One can therefore expect that the solutions for gap and displacement are (locally) similar for the different symmetries, except for pre- and scaling factors. In addition, percolation is continuous in the adhesion-free case, thereby constituting a critical point. Thus, there should exist (quasi-) universal functions for the various fields in the vicinity of the critical point, e.g., for the gap, on which we focus exemplarily. Following the ideas of the scaling hypothesis, the gap should then satisfy

$$g(l, x, y) = |l|^{\zeta} g^{\pm} \left(\frac{x}{|l|^{\chi}}, \frac{y}{|l|^{\nu}} \right) \quad (4)$$

where $l \equiv (L - L_c)/L_c$ is a reduced load, $g^{\pm}(\dots)$ denotes two master functions depending on the sign of l , while χ , ν , and ζ are universal scaling exponents. To superimpose the gap functions, not only for different values of l but also for different models — or more generally speaking for different curvature ratios $\eta \equiv -h''_{||}/h''_{\perp}$ characterizing the geometry of the saddle point — appropriate unit systems for x , y , and z need to be defined. For example, for the square lattice, or $\eta = 1$, a reasonable choice is to define the minimum width and minimum height of the open channel as 1 for $l = -0.01$ just like the length of the blocked channel for $l = 0.01$. For other geometries, or $\eta \neq 1$, the proper definition of units then depends on η and also on the sign of l .

Numerically, we see equation (4) to hold and demonstrate this in Figure 5. Specifically, in panel (a), contact lines obtained for different reduced loads and different geometries (exemplarily triangular and square) collapse onto their master curve that solely depends on the sign of l . Thus, all (near-) critical constrictions from Figure 4, lo-

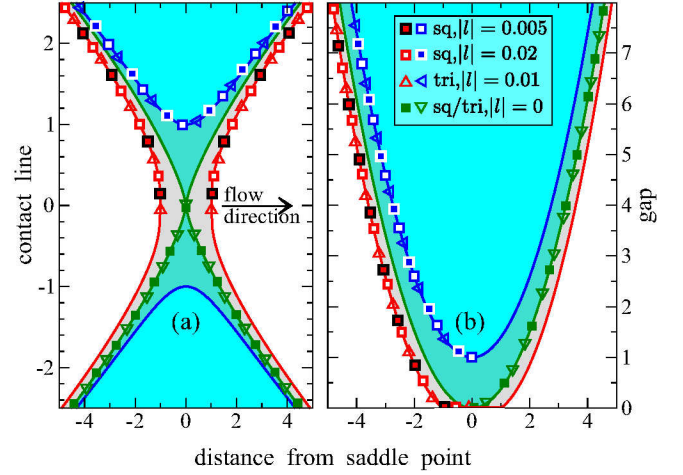


Fig. 5: (a) Contact line shape for normal loads below (blue), at (green), and, above (red) the critical load. (b) Gap on the symmetry axis as a function of the distance from the saddle point. Different symbols represent different saddle-point geometries and different colors different reduced loads l , as indicated in the caption. Solid areas and lines are obtained from analytical approximations to the contact shape. At a given value of l , distances are rescaled according to equation (4). Units are chosen such that gap height, length, and width are 1 for $|l| = 0.01$ in the square model.

cally adopt the contact line shapes from Figure 5 when viewed with sufficient magnification. Panel (b) shows that the gap can also be collapsed onto universal functions.

The numerical estimates for the exponents were obtained as follows: We first identified L_c as accurately as possible. We then ran simulations for $l = -0.002, -0.005, -0.01$, and -0.02 . By analyzing how the gap at the saddle point scales with l , the exponent ζ was determined to be $\zeta = 1.2 \pm 0.01$. The widths of the open channels were determined from the same set of simulations. The contact line positions, r_c , resulted from fitting the relation $F(r_{||} = 0, r_{\perp}) \propto \sqrt{r_{\perp} - r_c}$ to the forces exerted by the substrate onto the elastic body near the contact line. Here, the saddle point sat at $r_{||} = 0$ and $r_{\perp} = 0$ in the local coordinate system. This fitting procedure allowed us to determine the width of the open channel with sub-discretization resolution. All data was consistent with $\nu = 0.45 \pm 0.01$. To determine the length of blocked channels, simulations were run for positive reduced loads and the same absolute values of l as before. The pressure profile on the symmetry axis ($r_{||}, r_{\perp} = 0$) followed a Hertzian pressure profile very accurately, which allowed us to determine the length of the contact line on the symmetry axis to high precision and ultimately to ascertain that $\chi = 0.6 \pm 0.01$. Since the pressure profile on the contact ridges appears to be identical to that of a Hertzian contact, we believe that there exists an analytical solution, in which case, we would expect the exponents to be simple rational numbers — as in the Hertzian contact problem. We therefore speculate that $\chi = 3/5$, $\nu = 9/20$, and $\zeta = 6/5$ are the exact exponents.

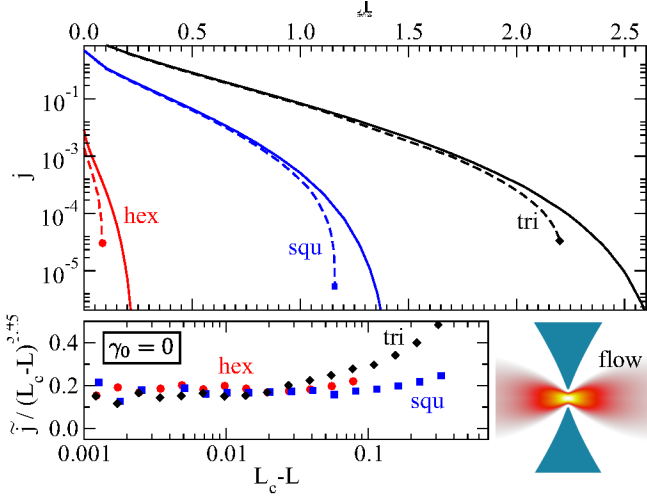


Fig. 6: **Top:** Fluid flow through the interface as a function of load. Solid lines refer to $\gamma_0 = 0$ and dashed lines to $\gamma_0 = 0.05$. The latter have end points, which are indicated by symbols. **Bottom left:** Normalized fluid flow as a function of $L_c - L$, in the non-adhesive case. **Bottom right:** Visualization of the Reynolds thin-film current density in the critical region.

Knowledge of the three exponents ζ , χ , and v allows one to deduce the power law with which Reynolds flow is suppressed as the load is increased toward L_c . Since the fluid-pressure gradient is non-negligible only near the critical constriction, the resistance to fluid flow is proportional to the length of the channel. Moreover, it is inversely proportional to the channel width and, according to the Reynolds equation, the third power of the channel height. Thus, the resistance scales as

$$R(L) \propto (L_c - L)^{-\beta} \quad (5)$$

with

$$\beta = 3\zeta + v - \chi, \quad (6)$$

and a numerical value of $\beta = 3.45$. Figure 6 confirms these expectations for the investigated adhesion-free surfaces: Near the percolation threshold, all three system disappear with the same power law, even if prefactors may differ substantially. The exponent of $\beta = 3.45$ is reproduced quite accurately by the flow simulations. In the critical regime, the (scaled) current density always looks like the flow shown in the bottom right of Figure 6.

The absolute flow through the contacts changes dramatically with the saddle point geometry even for fixed height spectra, in parts, of course, because the percolation point is so sensitive to the geometry. In other words, the leakage rate is strongly dependent on the curvature ratio η or the skewness s of the height distribution, potentially even more so than previously recognized [23], see also [24]. Specifically, the single-wavelength models have $\eta = (4, 1, 1/4)$ and $s = (-\sqrt{2/3}, 0, \sqrt{2/3})$ for hexagonal, square, and triangular lattices, respectively. In addition, just as the contact area is discontinuous at the percolation

transition, flow ceases and starts discontinuously with the closing or opening of the constrictions once adhesion is considered.

Our present analysis does not include plasticity, because it will mostly affect the points in earliest contact, namely the peak heights where the local pressures are highest. We are mostly concerned with the areas with the most tenuous contact, and lowest contact pressures. Lateral plastic material flow from the peaks might slightly alter the detailed shape of the saddle point but such effects are beyond the scope of the present work.

The most problematic approximations for the continuation of the power law down to the nanoscopic vicinity of the final constriction are most likely that we neglect to consider (i) the existence of a slip length (and the associated deviation from a Poiseuille flow profile), (ii) confinement-induced viscosity change (via the orientation of molecules), as well as (iii) the non-smoothness of surfaces at nano-scales (where the continuum approximation breaks down).

However, we note that shear-thinning does not come into play for the flow analysis, not even very close to the percolation threshold. This is because the maximum shear rate of a Poiseuille flow through a constriction is proportional to the gap height divided by the channel length. As a consequence, the maximum shear rate disappears with $l^{\zeta-\chi}$ with $\zeta - \chi \approx 0.6$, which we see confirmed by our simulation results.

Conclusions. – In this study we find that adjacent contact patches merge or break up discontinuously when finite-range interactions act in addition to hard-wall repulsion. This result has two main implications: First, in most cases, contact patches cannot be separated by a marginal distance or joined via arbitrarily thin ridges, which might explain why classical experiments [3] visualizing the contact between two nominally flat solids as well as recent computer simulations including adhesion [25] showed clearly separated contact patches, while large-scale simulations of *non-adhesive* solids [5–9] usually necessitate excessively high resolution to determine the connectedness of contact patches. Second, the contact-patch coalescence and break-up occur through first-order instabilities implying multistability. Thus, coalescence and break-up dynamics constitute a dissipation mechanism for Coulomb friction as any other instability induced by the relative sliding motion of two solids [26, 27]. Moreover, multistability entails thermal aging, which could be perceived as bulk relaxation and lead, for example, to a non-negligible time dependence of the leak rate of seals near percolation.

In reference to Persson’s contact mechanics [2] and his single-junction leak-rate theory [14], we also find two main implications. First, we demonstrate that the contact mechanics of surfaces with single-wavelength roughness and their leakage rate are highly sensitive to the way in which local maxima and minima are arranged. For example, our triangular and hexagonal models seal at very different

normal loads and relative contact areas, although the two geometries have identical height spectra. It might be possible to incorporate such effects — effectively representing a correlation of the phases for different $\tilde{h}(\mathbf{q})$ at fixed $|\mathbf{q}|$ — into the theory via appropriate generalizations. Second, in the absence of adhesion, we find that the length and the width of a constriction are not similar in magnitude as assumed in Ref. [14]. Instead they disappear with different power laws as L_c is approached.

When adhesion is absent, the contact mechanics of “well-behaved” saddle points shows universal behavior near the percolation point. There, the gap is entirely determined by the sign of the reduced load and scaling factors. Another aspect of the universal behavior is that the pressure profile on a newly-formed contact ridge along the transverse direction seems identical to that of a Hertzian contact. We therefore see the possibility for closed-form analytical solutions of the contact mechanics of a saddle point, even if formulating the boundary conditions could be difficult.

Finally, we find for idealized conditions frequently assumed in continuum approaches (zero slip length, no confinement effects on viscosity, hard-wall repulsion only) that the Reynolds flow through a critical constriction follows $(L_c - L)^\beta$ with $\beta = 3.45$. Since, for the given assumptions, most fluid pressure drops near a single constriction in the immediate vicinity of the percolation point [14], the leak rate of a seal that is pressed against a randomly rough macroscopic solid would depend on load with the same power law as the isolated constriction. Despite this knowledge it is quite difficult to predict the *absolute* current because the detailed topography of the last constriction has a tremendous effect on prefactors but is usually unknown. Still, the percolation exponent would result from local contact mechanics and not, as commonly assumed in the theory of percolation [28], from the disorder at large length scales. Whether the classical view is reestablished once adhesion is included remains to be seen.

* * *

We thank the Jülich Supercomputing Centre for computing time.

REFERENCES

- [1] BOWDEN F. P. and TABOR D., *Friction and Lubrication* (Wiley, New York) 1956.
- [2] PERSSON B. N. J., *J. Chem. Phys.*, **115** (2001) 3840.
- [3] DIETERICH J. H., *J. Geophys. Res.*, **84** (1979) 2161.
- [4] SWINGLER J. and LALECHOS A., *J. Phys. D: Appl. Phys.*, **42** (2009) 085304.
- [5] HYUN S., PEI L., MOLINARI J.-F. and ROBBINS M. O., *Phys. Rev. E*, **70** (2004) 026117.
- [6] PEI L., HYUN S., MOLINARI J.-F. and ROBBINS M. O., *J. Mech. Phys. Sol.*, **53** (2005) 2385.
- [7] CAMPAÑA C., *Phys. Rev. E*, **78** (2008) 026110.

- [8] CAMPAÑA C., PERSSON B. N. J. and MÜSER M. H., *J. Phys.: Condens. Matter*, **23** (2011) 085001.
- [9] PUTIGNANO C., AFFERRANTE L., CARBONE G. and G. DEMELIO, *J. Mech. Phys. Sol.*, **60** (2012) 973.
- [10] JOHNSON K., GREENWOOD J. and HIGGINSON J., *Int. J. Mech. Sci.*, **27** (1985) 383.
- [11] KRITHIVASAN V. and JACKSON R. L., *Tribol. Lett.*, **27** (2007) 31.
- [12] SCARAGGI M., CARBONE G., PERSSON B. N. J. and DINI D., *Soft Matter*, **7** (2011) 10395.
- [13] YASTREBOV V. A., ANCIAUX G. and MOLINARI J.-F., *Tribol. Lett.*, **56** (2014) 171.
- [14] LORENZ B. and PERSSON B. N. J., *EPL*, **86** (2009) 44006.
- [15] MAUGIS D., *J. Colloid Interface Sci.*, **150** (1992) 243.
- [16] MÜSER M. H., *Beilstein J. Nanotech.*, **5** (2014) 419.
- [17] CAMPAÑA C. and MÜSER M. H., *Phys. Rev. B*, **74** (2006) 075420.
- [18] DAPP W. B., PRODANOV N. and MÜSER M. H., *Tribol. Lett.*, **53** (2014) 433.
- [19] FALGOUT R., JONES J. and YANG U., *The design and implementation of hypre, a library of parallel high performance preconditioners* presented at *Numerical Solution of Partial Differential Equations on Parallel Computers* 2006.
- [20] SAAD Y. and SCHULTZ M. H., *SIAM J. Sci. Stat. Comput.*, **7** (1986) 856.
- [21] ASHBY S. F. and FALGOUT R. D., *Nucl. Sci. Eng.*, **124** (1996) 145.
- [22] DAPP W. B., LÜCKE A., PERSSON B. N. J. and MÜSER M. H., *Phys. Rev. Lett.*, **108** (2012) 244301.
- [23] LORENZ B. and PERSSON B. N. J., *EPL*, **90** (2010) 38002.
- [24] YASTREBOV V. A., ANCIAUX G. and MOLINARI J.-F., *Int. J. Solids Struct.*, **52** (2015) 83.
- [25] PASTEWKA L. and ROBBINS M. O., *Proc. Natl. Acad. Sci.*, **111** (2014) 3298.
- [26] PRANDTL L., *Z. Angew. Math. Mech.*, **8** (1928) 85.
- [27] MÜSER M. H., *Phys. Rev. Lett.*, **89** (2002) 224301.
- [28] STAUFFER D. and AHARONY A., *An Introduction to Percolation Theory* (CRC Press) 1991.